Chapter 3
Data Analysis for Nanomaterials: Effective Medium Approximation, Its Limits and Implementations

Josef Humlicek

Abstract We review here basic theoretical approaches to the optical response of nanostructured materials. We use the well established framework of Effective medium approximation (EMA) and discuss key issues of its use. The treatment of this extensive subject is adapted to the needs of ellipsometric/polarimetric measurements on nanostructured materials. In Sects. 3.1 and 3.2 we formulate the problems and establish notation. Then, we recall and discuss, in Sects. 3.3 and 3.4, several well-known formulae for the effective dielectric function. Sections 3.5 and 3.6 are devoted to a fairly detailed comparison of selected measured data with results of the EMA models. We also assess the uncertainties involved in the EMA approach by visualizing the differences between results of its different versions (Sect. 3.7) and by calculating the differences from exact solutions (Sect. 3.8). Finally, Sect. 3.9 is devoted to the discussion of possible resonant behaviour of EMA mixtures.

3.1 Introduction

Contemporary materials science provides a wealth of unique materials obtained by a fine (nanometer-sized) mixing of different components. An example of a fairly complex artificial nanostructure is shown in Fig. 3.1. Six layers of the nanoscale mixture of molybdenum and SiO_2, separated by very thin SiO_2 spacers (bright horizontal lines), are placed on the oxidized silicon substrate (the bottom part showing the segment of 100 nm of length) and capped with the topmost SiO_2 layer. Differ-

J. Humlicek (✉)
Central European Institute of Technology, Masaryk University Kamenice 735,
62500 Brno, Czech Republic
e-mail: humlicek@physics.muni.cz

J. Humlicek
Department of Condensed Matter Physics, Faculty of Science, Masaryk University Kotlářská 2,
61137 Brno, Czech Republic

M. Losurdo and K. Hingerl (eds.), *Ellipsometry at the Nanoscale*,
DOI: 10.1007/978-3-642-33956-1_3,

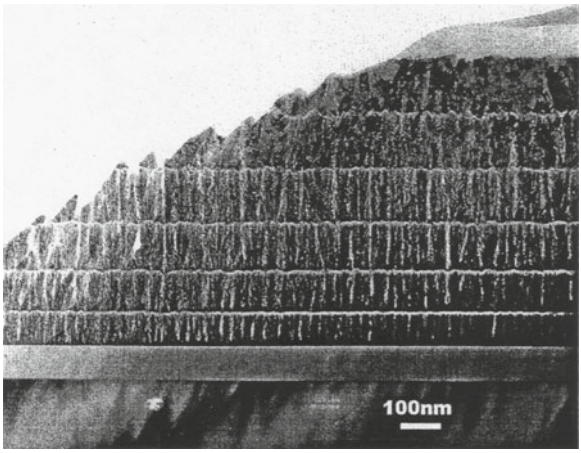

Fig. 3.1 TEM cross section of molybdenum/SiO_2 multilayer nanocomposite deposited on SiO_2/Si substrate. Courtesy of Ivo Vávra, Bratislava

ent deposition conditions of the individual Mo/SiO_2 layers were chosen in order to obtain different microstructures, seen as the changing contrast pattern of the transmission electron microscopy (TEM) picture. The targeted functionality of this kind of structures might be, for example, low-frequency electric conduction and/or optical behaviour in infrared/visible/ultraviolet range.

In general, many fundamental and functional properties of nanocomposites can be conveniently probed using several variants of optical spectroscopy. In particular, using polarized light in ellipsometric measurements proves to be highly efficient. The scheme of reflection and transmission of polarized optical wave interacting with slabs of nanostructured materials is shown in Figs. 3.2 and 3.3. The structure of Fig. 3.2 consists of thin layers extended in the (x,y) plane and stacked along the z-direction, which is typical of contemporary epitaxial heterostructures; that of Fig. 3.3 indicates small particles dispersed in a matrix.

Optical fields in the (meta)materials and the corresponding far-field solutions can be, in principle, obtained from rigorous full-wave analysis. This is usually very tedious, and the results are accompanied by a considerable volume of unwanted information. The fine structure of the optical fields is mostly irrelevant, since only smooth macroscopic averages are detected in actual measurements. Thus, the obvious replacement of mixed materials with "effective medium" can provide a plausible solution. This approach is usually termed EMA (effective medium approximation) or EMT (effective medium theory). The concept of EMA is very old; in fact, Maxwell included a paragraph on the electric conduction in a mixture in his famous *Treatise* [1].

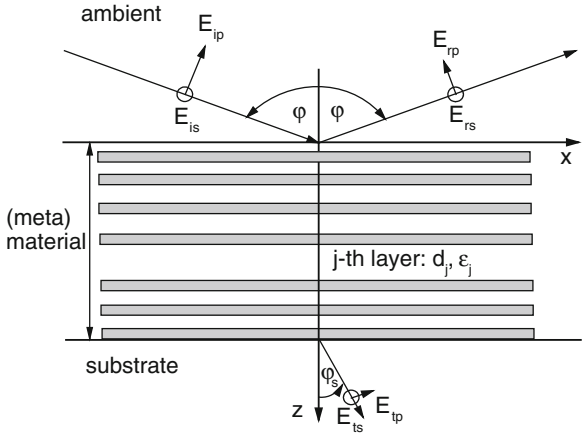

Fig. 3.2 Cross section of a planar ambient-film-substrate system. The film consists of a stack of different materials with interfaces parallel to the surface

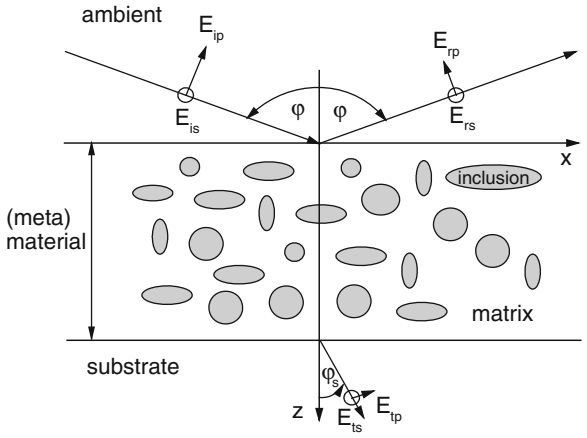

Fig. 3.3 Cross section of a planar ambient-film-substrate system. The film consists of nanoparticles embedded in a matrix material

3.2 Linear Optical Response of Nanostructured Materials

Optical frequencies, $\sim 3 \times 10^{11} - 3 \times 10^{16}$ Hz, cover the range from far-infrared (FIR) to vacuum-ultraviolet (VUV) spectral regions; the longest and shortest vacuum wavelength is about 1 mm and 10 nm, respectively. Since the atomic dimensions are of the order of 0.1 nm, matter behaves as a continuum at the optical frequencies and below (microwaves and radio waves). Namely, the wavelength is large enough to prevent substantial diffraction on the atomic structure, in contrast to the shorter wavelengths of the X-ray range. Although the discrete atomic structure of matter pro-

duces strong spatial variations of the quantities describing optical fields, the smooth averages at macroscopic length scales are usually detected using a light probe from the optical range.

The nanostructured materials are *mixtures* of individual components, possessing their own optical (continuum-like) behaviour. In other words, the atomic structure of individual components enters merely a limited number of macroscopic quantities, characteristic of the corresponding continuum. A second (sometimes called *mesoscopic*) level of averaging might be useful in representing the mixture as another continuum, with negligible diffraction on the mesoscopic structure. The possibility to use this continuum representation is not as universal as that of bulk materials, due to a wide range of possible sizes of the components.

The essential step in treating a mixture as a continuum consists in finding the macroscopic (averaged) field quantities. The actual behaviour of the mixture differs from this approximative treatment (effective medium approximation, EMA), whenever the structuring is not fine enough on the length scale of a single wavelength. Obviously, the fulfilment of this condition depends on the spectral range: a mesoscopic structure with characteristic dimensions of $\sim$10 nm is likely to behave as a continuum in infrared and visible, but not in ultraviolet.

Maxwell equations govern the spatial and temporal dependencies of the electromagnetic field:

$$\nabla \times \boldsymbol{E} = -\partial \boldsymbol{B}/\partial t, \quad \nabla \times \boldsymbol{H} = \partial \boldsymbol{D}/\partial t + \boldsymbol{j}, \quad \nabla \cdot \boldsymbol{D} = \boldsymbol{\rho}, \quad \nabla \cdot \boldsymbol{B} = 0. \quad (3.1)$$

The electric and magnetic field quantities and their units in the SI system are the following vectors: $\boldsymbol{E}$ [V/m], the electric intensity, $\boldsymbol{H}$ [A/m], the magnetic intensity, $\boldsymbol{D}$ [As/m^2], the electric displacement (flux density), $\boldsymbol{B}$ [Vs/m^2], the magnetic displacement (flux density), $\boldsymbol{j}$ [A/m^2], the current density. The scalar ρ [As/m^3] is the charge density.

The linear response of matter to the monochromatic electromagnetic field, where all of the quantities follow the harmonic time dependence of $\exp(-\mathrm{i}\omega t)$ with the angular frequency ω, is described by the *constitutive relations* for the displacements and intensities,

$$\boldsymbol{D} = \varepsilon(\omega)\varepsilon_0 \boldsymbol{E}, \quad \boldsymbol{B} = \mu_0 \boldsymbol{H}, \quad (3.2)$$

where $\varepsilon_0 = 8.85 \times 10^{-12}$ As/Vm is the vacuum permittivity, $\mu_0 = 4\,\pi \times 10^{-7}$ Vs/Am the vacuum permeability, and $\varepsilon(\omega)$ the (dimensionless) relative permittivity. Alternatively, the induced current density $\boldsymbol{j}$ is a linear function of the electric intensity and the proportionality factor, the conductivity σ, is simply related to the permittivity:

$$\boldsymbol{j} = \sigma(\omega)\boldsymbol{E}, \quad \sigma(\omega) = -i\omega[\varepsilon(\omega) - 1]\varepsilon_0. \quad (3.3)$$

The SI unit of conductivity is A/Vm = 1/Ωm. The linear response of Eqs. (3.2) and (3.3) contains complex functions of frequency, $\varepsilon = \varepsilon_1 + i\varepsilon_2$ and $\sigma = \sigma_1 + i\sigma_2$,

reflecting possible phase shifts between the electric field and the induced polarization/current at finite frequencies. The second of equations (3.3) is a simple consequence of the indistinguishability of $\partial \boldsymbol{D}/\partial t$ and $\boldsymbol{j}$ in the second of Maxwell equation (3.1) at optical frequencies.

As usual, we use the complex permittivity as the preferred response function. However, the complex conductivity might be more appropriate for conducting structures in IR.

3.3 Average Fields and Effective Permittivity for a Small Contrast

A simple approach to the dielectric response of a mixture is due to Landau-Lifshitz [2]. The mixture is assumed to be finely dispersed, representing a homogeneous and isotropic material with respect to the macroscopic field. Its effective permittivity relates the volume-averaged displacement and intensity,

$$\langle \boldsymbol{D} \rangle = \varepsilon_{\mathit{eff}} \langle \boldsymbol{E} \rangle, \tag{3.4}$$

where the averaging volume V has to be large enough to be representative of the mixture, and, in optical case, small in comparison with the wavelength. Using the averages of the intensity and permittivity,

$$\langle \boldsymbol{E} \rangle = (1/V) \int \boldsymbol{E}(\boldsymbol{r}) dxdydz, \quad \langle \varepsilon \rangle = (1/V) \int \varepsilon(\boldsymbol{r}) dxdydz, \tag{3.5}$$

the local field intensity and permittivity at the position $\boldsymbol{r} = (x, y, z)$ can be written as

$$\boldsymbol{E}(\boldsymbol{r}) = \langle \boldsymbol{E} \rangle + \boldsymbol{\delta E}(\boldsymbol{r}), \quad \varepsilon(\boldsymbol{r}) = \langle \varepsilon \rangle + \delta\varepsilon(\boldsymbol{r}). \tag{3.6}$$

The essential step in calculating the mean displacement,

$$\langle \boldsymbol{D} \rangle = \langle (\langle \varepsilon \rangle + \boldsymbol{\delta}\varepsilon(\boldsymbol{r}))(\langle \boldsymbol{E} \rangle + \boldsymbol{\delta E}(\boldsymbol{r})) \rangle = \langle \varepsilon \rangle \langle \boldsymbol{E} \rangle + \langle \boldsymbol{\delta}\varepsilon(\boldsymbol{r}) \boldsymbol{\delta E}(\boldsymbol{r})) \rangle, \tag{3.7}$$

consists in finding the average of the product $\boldsymbol{\delta}\varepsilon(\boldsymbol{r})\boldsymbol{\delta E}(\boldsymbol{r})$. An approximate treatment of Landau-Lifshitz uses the third of Maxwell equation (3.1) with the vanishing charge density ρ, which relates the divergence of the displacement to positional dependencies of the field intensity and permittivity:

$$\begin{aligned} \nabla \cdot \boldsymbol{D} &= \nabla \cdot [(\langle \varepsilon \rangle + \delta\varepsilon(\boldsymbol{r}))(\langle \boldsymbol{E} \rangle + \delta \boldsymbol{E}(\boldsymbol{r}))] \\ &\approx \langle \varepsilon \rangle \nabla \cdot [\delta \boldsymbol{E}(\boldsymbol{r})] + \langle \boldsymbol{E} \rangle \nabla \cdot [\delta\varepsilon(\boldsymbol{r})] = 0. \end{aligned} \tag{3.8}$$

The divergence of the product $\delta\varepsilon(\boldsymbol{r})\delta\boldsymbol{E}(\boldsymbol{r})$ is supposed to be negligible. The second term of the right-hand side of Eq. (3.7) is calculated in two steps. First, the spatial average is performed over the regions of constant $\delta\varepsilon$, i.e., for a given component of the mixture. The corresponding average of $\delta\boldsymbol{E}$ can be obtained from its divergence

$$\nabla\cdot\langle\delta\boldsymbol{E}(\boldsymbol{r})\rangle = \frac{\delta}{\delta x}\langle\delta E_x(\boldsymbol{r})\rangle + \frac{\delta}{\delta y}\langle\delta E_y(\boldsymbol{r})\rangle + \frac{\delta}{\delta z}\langle\delta E_z(\boldsymbol{r})\rangle = 3\frac{\delta}{\delta x}\langle\delta E_x(\boldsymbol{r})\rangle, \quad (3.9)$$

using the assumption of the isotropy of the 3-dimensional mixture. Choosing the direction of $\langle\boldsymbol{E}\rangle$ along x, we obtain from Eq. (3.8) the following relations,

$$3\langle\varepsilon\rangle\frac{\delta}{\delta x}\langle\delta E_x(\boldsymbol{r})\rangle = -\langle E_x(\boldsymbol{r})\rangle\frac{\delta}{\delta x}\langle\varepsilon(\boldsymbol{r})\rangle, \quad \langle\delta\boldsymbol{E}(\boldsymbol{r})\rangle = -\frac{1}{3\langle\varepsilon(\boldsymbol{r})\rangle}\langle\boldsymbol{E}(\boldsymbol{r})\rangle\delta\varepsilon(\boldsymbol{r}). \quad (3.10)$$

The second stage of finding the average of Eq. (3.7) is performed by multiplying the second of Eq. (3.10) by $\delta\varepsilon$, and averaging over all species in the mixture. The result reads

$$\langle\delta\varepsilon(\boldsymbol{r})\delta\boldsymbol{E}(\boldsymbol{r})\rangle = -\frac{1}{3\langle\varepsilon(\boldsymbol{r})\rangle}\langle\boldsymbol{E}(\boldsymbol{r})\rangle\langle(\delta\varepsilon(\boldsymbol{r}))^2\rangle. \quad (3.11)$$

Using this in Eqs. (3.7) and (3.4), we find the resulting effective permittivity,

$$\varepsilon_{eff} = \langle\varepsilon\rangle - \frac{\langle(\delta\varepsilon)^2\rangle}{3\langle\varepsilon\rangle}. \quad (3.12)$$

We call the result of Eq. (3.12) the Landau-Lifshitz (LL) formula. It can be expressed approximately in the following appealing way. Neglecting higher-order terms in the third power of the Taylor expansion of the averaged cube root,

$$\langle\varepsilon^{1/3}\rangle^3 = \langle(\langle\varepsilon\rangle + \delta\varepsilon)^{1/3}\rangle^3 \approx \langle\varepsilon\rangle - 3\langle\varepsilon\rangle\frac{1\cdot 2}{3\cdot 6}\frac{\langle(\delta\varepsilon)^2\rangle}{\langle\varepsilon\rangle^2}, \quad (3.13)$$

the right-hand side of Eq. (3.12) is recovered, i.e.,

$$\varepsilon_{eff} = \langle\varepsilon^{1/3}\rangle^3. \quad (3.14)$$

This form of the approximate effective permittivity has been obtained in a different way by Looyenga [3]; the formula of Eq. (3.14) is sometimes labeled as LLL (Landau-Lifshitz-Looyenga). In practice, it does not bring any essential advantage compared with the LL formula of Eq. (3.12).

The above development can be easily modified for structures of lower dimensions. Let us assume translational invariance of the mixture along one spatial dimension (z), with the structuring restricted to the (x,y) plane of the 2-dimensional (2D) system. The material is uniaxial, with the optical axis along z, and the z (extraordinary) component

of its dielectric tensor equals the volume average $\langle\varepsilon\rangle$. In order to calculate the ordinary component, we notice that the divergence of Eq. (3.9) becomes

$$\nabla\cdot\langle\delta\boldsymbol{E}(\boldsymbol{r})\rangle=\frac{\delta}{\delta x}\langle\delta E_x(\boldsymbol{r})\rangle+\frac{\delta}{\delta y}\langle\delta E_y(\boldsymbol{r})\rangle=2\frac{\delta}{\delta x}\langle\delta E_x(\boldsymbol{r})\rangle. \tag{3.15}$$

Similarly, with the structuring vanishing along z and y in a one-dimensional (1D) mixture, the material is uniaxial with the optical axis along x, and the y and z (ordinary) components of the dielectric tensor are equal to the volume average $\langle\varepsilon\rangle$. The divergence of Eq. (3.9) is reduced to

$$\nabla\cdot\langle\delta\boldsymbol{E}(\boldsymbol{r})\rangle=\frac{\delta}{\delta x}\langle\delta E_x(\boldsymbol{r})\rangle. \tag{3.16}$$

The corresponding modification of the corresponding tensor components of the effective permittivity of Eq. (3.12) is

$$\varepsilon_{eff}=\langle\varepsilon\rangle-\frac{\langle(\delta\varepsilon)^2\rangle}{D\langle\varepsilon\rangle}, \tag{3.17}$$

where D =3, 2, 1 for the 3D, 2D, and 1D mixtures, respectively.

Let us note that looking for an approximate representation of Eq. (3.17) using powers, analogous to Eq. (3.14), leads to the following simple result in the 1-dimensional ($D=1$) case: the right-hand side of Eq. (3.17) is recovered when expanding

$$\varepsilon_{eff}|_{1\mathrm{D}}=\langle\varepsilon^{-1}\rangle^{-1}. \tag{3.18}$$

This is actually a precise result of the long-wavelength averaging for general lamellar structures, not restricted to the low contrast of constituents. We will use this fact later in order to test the level of errors introduced by the assumption of the small contrast.

For the simplest mixture consisting of just two components, a and b, the averages can be expressed explicitly in terms of their permittivities, ε_a and ε_b, and the volume fractions, f_a and f_b,

$$f_a=V_a/(V_a+V_b),\quad f_b=V_b/(V_a+V_b)=1-f_a\equiv f. \tag{3.19}$$

Thus, the composition of binary mixtures is specified by a single parameter f, the volume fraction of the component occupying volume V_b, with the permittivity of ε_b. The average permittivity of the binary mixture is

$$\langle\varepsilon\rangle=(1-f)\varepsilon_a+f\varepsilon_b=\varepsilon_a+f(\varepsilon_b-\varepsilon_a), \tag{3.20}$$

the deviations from the mean are

$$\delta\varepsilon_a=\varepsilon_a-\langle\varepsilon\rangle=f(\varepsilon_a-\varepsilon_b),\quad \delta\varepsilon_b=\varepsilon_b-\langle\varepsilon\rangle=(1-f)(\varepsilon_b-\varepsilon_a), \tag{3.21}$$

the mean of the squared deviation is

$$\langle(\delta\varepsilon)^2\rangle = (1-f)(\delta\varepsilon_a)^2 + f(\delta\varepsilon_b)^2 = f(1-f)(\varepsilon_b-\varepsilon_a)^2, \tag{3.22}$$

and the LL formula of Eq. (3.17) reads

$$\varepsilon_{eff} = \varepsilon_a + f(\varepsilon_b-\varepsilon_a) - \frac{f(1-f)(\varepsilon_b-\varepsilon_a)^2}{D[\varepsilon_a + f(\varepsilon_b-\varepsilon_a)]}. \tag{3.23}$$

The approximation based on neglecting higher-order terms in the derivation of Eqs. (3.8)–(3.17) introduces differences that are, in general, difficult to specify. We will discuss these errors later, using partly precise solutions for selected 1D cases, partly comparisons with predictions of the effective dielectric functions that do not assume the low contrast.

3.4 A Collection of Mixing Rules

A mixture is isotropic in the absence of preferred directions of polarization on macroscopic scale. This condition is evidently not fulfilled in cases of preferential orientations of the interfaces between the components. Two extreme cases of the orientation of aligned *planar* interfaces with respect to the direction of electric field can easily be identified; they are shown in Fig. 3.4.

Applying the boundary conditions for tangential and normal components of $\boldsymbol{E}$ and $\boldsymbol{H}$ [4], the two orientations differ in the average values of the field quantities. Namely, $\boldsymbol{E}_a = \boldsymbol{E}_b = \langle\boldsymbol{E}\rangle$ in the parallel case, leading to the following average value of the displacement,

$$\langle\boldsymbol{D}\rangle = (1-f)\varepsilon_a\boldsymbol{E}_a + f\varepsilon_b\boldsymbol{E}_b = [(1-f)\varepsilon_a + f\varepsilon_b]\langle\boldsymbol{E}\rangle, \tag{3.24}$$

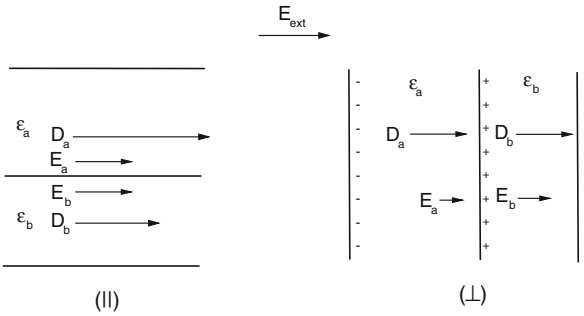

Fig. 3.4 Cross sections of a layered structure with the parallel (*left part*, no screening charges at the interfaces) and perpendicular (*right part*, maximum screening charge density) orientation with respect to the electric field

where f is the volume fraction of the component b. Thus, the effective permittivity of Eq. (3.4) is the simple volume average of the two components,

$$\varepsilon_{eff} = \langle \varepsilon \rangle = (1 - f)\varepsilon_a + f\varepsilon_b. \tag{3.25}$$

On the other hand, normal components of the displacement $\boldsymbol{D}$ are continuous ($\boldsymbol{D}_a = \boldsymbol{D}_b = \langle \boldsymbol{D} \rangle$) across the interfaces in the perpendicular case, leading to the following average value of the electric intensity perpendicular to the planes,

$$\langle \boldsymbol{E} \rangle = (1 - f)\boldsymbol{D}_a/\varepsilon_a + f\boldsymbol{D}_b/\varepsilon_b = [(1 - f)/\varepsilon_a + f/\varepsilon_b]\langle \boldsymbol{D} \rangle. \tag{3.26}$$

Consequently, the inverse of the effective permittivity along the horizontal direction is the volume average of the inverses of the permittivities of the individual components (i.e., the inverse permittivity is additive),

$$1/\varepsilon_{eff} = (1 - f)/\varepsilon_a + f/\varepsilon_b. \tag{3.27}$$

The two orientations of layers in Fig. 3.4. differ in the absence/presence of screening charges at the interfaces. Namely, a surface charge density develops at the interfaces in the perpendicular case, which is related to the discontinuity of the electric field intensity across the interface. On the other hand, no screening charges appear in the parallel case. Curved interfaces lead evidently to more complex field patterns, with positional dependence of the surface charge density.

The case of a *spherical* (more generally, ellipsoidal) inclusion is particularly simple, as it allows an analytical solution [5]. Shown in Fig. 3.5 are the field lines describing the field in and around a dielectric sphere. The inner field, produced by the applied intensity and screening charges unevenly distributed on the surface, is constant [4]:

$$E_b = \frac{3\varepsilon_a}{\varepsilon_b + 2\varepsilon_a} E_a. \tag{3.28}$$

Note that the inner field is weaker than the outer one for $\varepsilon_b > \varepsilon_a$, i.e., for the inclusion more polarizable than the host material (if both permittivities are real). Static fields are assumed in calculations of average quantities; however, the optical case is essentially the same for the diameter of the sphere negligible with respect to the wavelength and the penetration depth of light.

The more general case of an ellipsoid leads to similar results. Let us assume an ellipsoid (permittivity ε_b, semi axes u, v, and w) with u oriented along the electric field intensity. The field inside the ellipsoid is constant [5],

$$E_b = \frac{\varepsilon_a}{(1 - L_u)\varepsilon_a + L_u\varepsilon_b} E_a, \tag{3.29}$$

where

$$L_u = \frac{uvw}{2} \int_0^\infty \frac{dt}{(t^2+u^2)\sqrt{(t+u^2)(t+v^2)(t+w^2)}} \in \langle 0, 1\rangle \tag{3.30}$$

is the *depolarization factor*. The three depolarization factors of any ellipsoid satisfy the condition $L_u + L_v + L_w = 1$. Special cases are

$$L_u = L_v = L_w = \frac{1}{3} \quad \text{for } u = v = w \quad \text{(sphere)}, \tag{3.30a}$$

$$L_u = L_v = \frac{1}{2}, L_w = 0 \quad \text{for } u = v, w \to \infty \quad \text{(cylinder)}, \tag{3.30b}$$

$$L_u = 1, L_v = L_w = 0 \quad \text{for } v = w \to \infty \quad \text{(slab)}. \tag{3.30c}$$

Note that the zero depolarization inserted into Eq. (3.29) reproduces the condition $E_a = E_b$ for the interface parallel to the field; this occurs for the orientation of a cylinder or a slab with the interfaces parallel to the field. On the other hand, the maximum (unit) value of the depolarization factor describes the continuity of the normal component of electric displacement, $\varepsilon_a E_a = \varepsilon_b E_b$, for a slab with its normal oriented along the field.

The simplest version of averaging the microscopic fields (such as those in Fig. 3.5) neglects the dipole-like field pattern in the close neighborhood of the spheres, sparsely dispersed in the host material. Using the volume fraction f of the spheres, the average intensity and displacement is approximately

$$\langle E\rangle \approx (1-f)E_a + fE_b = \left[1 - f + \frac{f3\varepsilon_a}{\varepsilon_b + 2\varepsilon_a}\right] E_a, \tag{3.31a}$$

$$\langle D\rangle \approx (1-f)\varepsilon_a E_a + f\varepsilon_b E_b = \left[(1-f)\varepsilon_a + \frac{f3\varepsilon_a\varepsilon_b}{\varepsilon_b + 2\varepsilon_a}\right] E_a. \tag{3.31b}$$

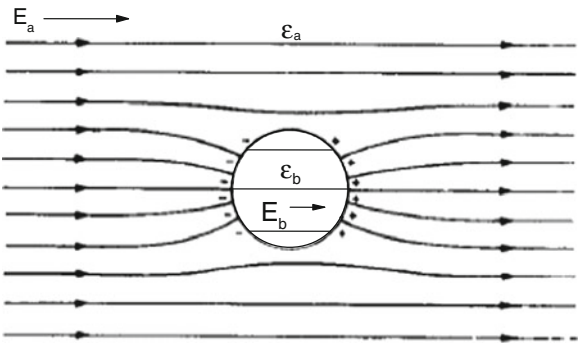

Fig. 3.5 A dielectric sphere embedded in an infinite dielectric medium under the electric field E_a

The effective dielectric function of Eq. (3.4) is then given by the well known Maxwell Garnett [6] formula

$$\varepsilon_{eff} = \frac{\langle D \rangle}{\langle E \rangle} = \varepsilon_a + f(\varepsilon_b - \varepsilon_a)\frac{3\varepsilon_a}{\varepsilon_b + 2\varepsilon_a - f(\varepsilon_b - \varepsilon_a)}. \tag{3.32}$$

This result explained colors in glasses with nanometer-sized spherical metallic inclusions as early as in 1904.

The Maxwell Garnett (MG) formula is easily generalized to a dilute mixture of aligned ellipsoids in a host matrix as

$$\varepsilon_{eff,u} = \varepsilon_a + f(\varepsilon_b - \varepsilon_a)\frac{\varepsilon_a}{\varepsilon_a + L_u(1-f)(\varepsilon_b - \varepsilon_a)}. \tag{3.32a}$$

A mixture with randomly oriented ellipsoids is isotropic, with the scalar permittivity

$$\varepsilon_{eff} = \varepsilon_a + f(\varepsilon_b - \varepsilon_a)\varepsilon_a \frac{\sum\limits_{j=u,v,w} 1/[\varepsilon_a + L_j(\varepsilon_b - \varepsilon_a)]}{3 - f(\varepsilon_b - \varepsilon_a)\sum\limits_{j=u,v,w} L_j/[\varepsilon_a + L_j(\varepsilon_b - \varepsilon_a)]}. \tag{3.32b}$$

Two limiting cases of very prolate and oblate ellipsoids are useful; the cylinders of Eq. (3.30b) are likely to approximate the behavior of needle-like inclusions, with the effective permittivity of the random orientation

$$\varepsilon_{eff} = \varepsilon_a + f(\varepsilon_b - \varepsilon_a)\frac{\varepsilon_b + 5\varepsilon_a}{3(\varepsilon_b + \varepsilon_a) + 2f(\varepsilon_a - \varepsilon_b)}. \tag{3.32c}$$

Using the depolarization factors of Eq. (3.30c), we obtain the effective permittivity of disk- or platelet-shaped inclusions with random orientation,

$$\varepsilon_{eff} = \varepsilon_a + f(\varepsilon_b - \varepsilon_a)\frac{2\varepsilon_b + 2\varepsilon_a}{3\varepsilon_b + f(\varepsilon_a - \varepsilon_b)}. \tag{3.32d}$$

An instructive treatment of mixtures can be based on a simplified *microscopic* model, with the polarization of components represented by point dipoles [7]. For simple geometries, the average values can be found analytically, and the distinction between local field causing the polarization and experimentally accessible macroscopic (averaged) field is straightforward. On the other hand, the actual induced density of dipole moment of either electrons or atomic nuclei in condensed matter is significantly different from the diverging pattern of point dipoles. A discrete set of dipoles of different polarizabilities, representing two different materials, leads to the effective dielectric function obeying the equation

$$f\frac{\varepsilon_b - 1}{\varepsilon_b + 2} + (1-f)\frac{\varepsilon_a - 1}{\varepsilon_a + 2} = \frac{\varepsilon_{eff} - 1}{\varepsilon_{eff} + 2}. \tag{3.33}$$

Evidently, it can be viewed as a variant of Clausius-Mosotti or Lorentz–Lorenz relation [7]. It is actually of the same form as the Maxwell Garnett formula (3.32); the latter can easily be put in the form

$$f\frac{\varepsilon_b-\varepsilon_a}{\varepsilon_b+2\varepsilon_a}=\frac{\varepsilon_{eff}-\varepsilon_a}{\varepsilon_{eff}+2\varepsilon_a}. \tag{3.34}$$

In fact, introducing the permittivity ε_h of the *host material*, the following general form

$$f\frac{\varepsilon_b-\varepsilon_h}{\varepsilon_b+2\varepsilon_h}+(1-f)\frac{\varepsilon_a-\varepsilon_h}{\varepsilon_a+2\varepsilon_h}=\frac{\varepsilon_{eff}-\varepsilon_h}{\varepsilon_{eff}+2\varepsilon_h} \tag{3.35}$$

covers the Lorentz–Lorenz formula of Eq. (3.33) when taking $\varepsilon_h = 1$ (vacuum), and the Maxwell Garnett formula of Eq. (3.34) with $\varepsilon_h = \varepsilon_a$ (precisely in the spirit of the approximate calculations of the averages of Eq. (3.31a,b). An appealing variant of the mixing is to assume the host material to be the effective medium itself, $\varepsilon_h = \varepsilon_{eff}$. This was suggested by Bruggeman [8], resulting in the mixing formula

$$f\frac{\varepsilon_b-\varepsilon_{eff}}{\varepsilon_b+2\varepsilon_{eff}}+(1-f)\frac{\varepsilon_a-\varepsilon_{eff}}{\varepsilon_a+2\varepsilon_{eff}}=0. \tag{3.36}$$

The effective permittivity solves the following quadratic equation, with one of its two roots being physical,

$$2\varepsilon_{eff}^2+\varepsilon_{eff}\left[(3f-2)\varepsilon_a+(1-3f)\varepsilon_b\right]-\varepsilon_a\varepsilon_b=0. \tag{3.37}$$

The Bruggeman formula is symmetric with respect to interchanging the components, which is attractive for dealing with materials of comparable volume fractions in the mixture. Further, the way of its derivation leads to the expectation of a better performance outside the dilute limit of Maxwell Garnett formula.

Another attractive mixing rule is known as the coherent potential formula; we recall the form for spherical inclusions [9],

$$\varepsilon_{eff}=\varepsilon_a+f(\varepsilon_b-\varepsilon_a)\frac{3\varepsilon_{eff}}{3\varepsilon_{eff}+(1-f)(\varepsilon_b-\varepsilon_a)}. \tag{3.38}$$

As in the case of Bruggeman formula, the effective permittivity solves a quadratic equation, with only one of its two roots being physical:

$$3\varepsilon_{eff}^2+\varepsilon_{eff}\left[4(f-1)\varepsilon_a+(1-4f)\varepsilon_b\right]-(1-f)\varepsilon_a(\varepsilon_b-\varepsilon_a)=0. \tag{3.39}$$

We use here the label CPA (coherent potential approximation) for the mixing formula of Eq. (3.26). It is based, like the Bruggeman formula, on the assumption of the spherical form of inclusions. However, the averaging procedure of field quantities is different. For dilute mixtures of spheres ($f \ll 1$), both Bruggeman and CPA rules

give the same expansion to the first order in f as the Maxwell Garnett formula, namely

$$\varepsilon_{eff} \approx \varepsilon_a + f(\varepsilon_b - \varepsilon_a)\frac{3\varepsilon_a}{\varepsilon_b + 2\varepsilon_a}. \tag{3.40}$$

For real permittivities, the slope of this linear approximation is smaller than that of the linear interpolation between ε_a and ε_b for $\varepsilon_b > \varepsilon_a$ and vice versa. This is easily understandable with the help of the approximate averaging used in deriving the Maxwell Garnett rule above. It should be noted that the corresponding expansion found from Eq. (3.12),

$$\varepsilon_{eff} \approx \varepsilon_a + f(\varepsilon_b - \varepsilon_a)\frac{4\varepsilon_a - \varepsilon_b}{3\varepsilon_a}, \tag{3.41}$$

and (3.14),

$$\varepsilon_{eff} \approx \varepsilon_a + 3f(\varepsilon_a^{2/3}\varepsilon_b^{1/3} - \varepsilon_a), \tag{3.42}$$

is different from that of Eq. (3.40). This is not surprising, because of different assumptions used in deriving the latter two mixing rules. In fact, the most important requirement was a small contrast of the permittivities. No specific geometry of the mixture has been used; it should not be expected that the result valid for spherical inclusions would be obtained.

The EMA calculations done for the spherical inclusions can be easily modified for aligned ellipsoids, similar to the Maxwell Garnett type of averaging of Eq. (3.32a). The resulting effective medium is anisotropic, since the screening effects depend on the relative orientation of the electric field and the ellipsoids. An instructive case is that of the aligned cylinders, i.e., infinitely elongated ellipsoids with a circular cross-section. There is no screening for the field parallel to the cylinders, and the corresponding tensor component of the effective permittivity is just the volume average of Eq. (3.25). For the field perpendicular to a dilute system of cylinders, the two-dimensional distribution of screening charges leads to the following effective permittivity, which is a modification of Eq. (3.34),

$$f\frac{\varepsilon_b - \varepsilon_a}{\varepsilon_b + \varepsilon_a} = \frac{\varepsilon_{eff} - \varepsilon_a}{\varepsilon_{eff} + \varepsilon_a}, \tag{3.43}$$

sometimes called Rayleigh mixing formula. Obviously, Maxwell Garnett and Rayleigh mixing rules are two intermediate stages between the absence and maximum of screening in Eqs. (3.25) and (3.27), respectively.

Most of the rules for binary mixtures discussed above can be rewritten in the form of explicit relations for the volume fraction f. This is convenient, since the typical use of the effective medium approach is to estimate the composition from the known permittivities of the components, and the measured value for the mixture. We list in the table below several mixing formulas using the expression for the effective permittivity and the volume fraction (Table 3.1).

Table 3.1 Effective medium rules for binary mixtures

Effective medium	ε_{eff}	f
Layer stack, planes parallel to $\boldsymbol{E}$	$(1-f)\varepsilon_a + f\varepsilon_b$	$\dfrac{\varepsilon_{eff}-\varepsilon_a}{\varepsilon_b-\varepsilon_a}$
Layer stack, planes perp. to $\boldsymbol{E}$	$\dfrac{\varepsilon_a\varepsilon_b}{(1-f)\varepsilon_b + f\varepsilon_a}$	$\dfrac{\varepsilon_{eff}-\varepsilon_a}{\varepsilon_b-\varepsilon_a}\dfrac{\varepsilon_b}{\varepsilon_{eff}}$
LLL (small contrast)	$[(1-f)\varepsilon_a^{1/3} + f\varepsilon_b^{1/3}]^3$	$\dfrac{\varepsilon_{eff}^{1/3}-\varepsilon_a^{1/3}}{\varepsilon_b^{1/3}-\varepsilon_a^{1/3}}$
Maxwell Garnett (dilute spheres)	$\varepsilon_a + f(\varepsilon_b-\varepsilon_a)\dfrac{3\varepsilon_a}{\varepsilon_b+2\varepsilon_a-f(\varepsilon_b-\varepsilon_a)}$	$\dfrac{\varepsilon_{eff}-\varepsilon_a}{\varepsilon_b-\varepsilon_a}\dfrac{\varepsilon_b+2\varepsilon_a}{\varepsilon_{eff}+2\varepsilon_a}$
Rayleigh (dilute cylinders)	$\varepsilon_a + f(\varepsilon_b-\varepsilon_a)\dfrac{2\varepsilon_a}{\varepsilon_b+\varepsilon_a-f(\varepsilon_b-\varepsilon_a)}$	$\dfrac{\varepsilon_{eff}-\varepsilon_a}{\varepsilon_b-\varepsilon_a}\dfrac{\varepsilon_b+\varepsilon_a}{\varepsilon_{eff}+\varepsilon_a}$
Maxwell Garnett (dilute aligned ellipsoids)	$\varepsilon_a + f(\varepsilon_b-\varepsilon_a)\dfrac{\varepsilon_a}{\varepsilon_a+L(1-f)(\varepsilon_b-\varepsilon_a)}$	$\dfrac{\varepsilon_{eff}-\varepsilon_a}{\varepsilon_b-\varepsilon_a}\dfrac{\varepsilon_a+L(\varepsilon_b-\varepsilon_a)}{\varepsilon_a+L(\varepsilon_{eff}-\varepsilon_a)}$
Bruggeman (spheres)	$2\varepsilon_{eff}^2 + \varepsilon_{eff}[(3f-2)\varepsilon_a + (1-3f)\varepsilon_b] - \varepsilon_a\varepsilon_b = 0$	$\dfrac{\varepsilon_{eff}-\varepsilon_a}{\varepsilon_b-\varepsilon_a}\dfrac{\varepsilon_b+2\varepsilon_{eff}}{3\varepsilon_{eff}}$
CPA (spheres)	$3\varepsilon_{eff}^2 + \varepsilon_{eff}[4(f-1)\varepsilon_a + (1-4f)\varepsilon_b] - (1-f)\varepsilon_a(\varepsilon_b-\varepsilon_a) = 0$	$\dfrac{\varepsilon_{eff}-\varepsilon_a}{\varepsilon_b-\varepsilon_a}\dfrac{3\varepsilon_{eff}+\varepsilon_b-\varepsilon_a}{4\varepsilon_{eff}-\varepsilon_a}$

The volume fraction of the component a is $1-f$, that of the component b is f. L is the depolarization factor of Eq. (3.30). For the Bruggeman and CPA models the effective permittivity results from the solution of the quadratic equation given in the table

3.5 Tests of EMA: Glass Spheres in Liquids

An illustrative example of using different mixing formulas is the system of glass spheres dispersed in liquids. The effective response has been studied experimentally in the low (≤GHz) frequency range, using the mixture as a dielectric in a condenser or a resonator. Even fairly large glass particles (mostly spheres) warrant the applicability of the continuum approach, since the vacuum wavelength λ_{vac} at the frequency of 1 GHz is 0.3 m and the effective refractive index of the mixture, $n_{eff} = \sqrt{(\varepsilon_{eff})}$, does not exceed 10. Thus, the diameter of the glass spheres, smaller than about 1 mm, is much smaller than the wavelength in the effective medium, λ_{vac}/n_{eff}.

First, we analyze the mixture of glass spheres in the non-polar liquid of carbon tetrachloride; the experimental results of J. A. Reynolds quoted in [3] are shown in Fig. 3.6, together with the long-wavelength (real) permittivity predicted by four selected mixing formulas as a function of the volume fraction f of glass. A slightly bowed dependence is almost coinciding for Bruggeman, Eq. (3.36), Landau-Lifshitz-Looyenga, Eq. (3.14), and CPA, Eq. (3.38), formulas. The prediction of Maxwell Garnett, Eq. (3.32), lies slightly below the three.

Since the mutual differences of the mixing formulas are rather small, we show their differences from the Bruggeman model in Fig. 3.7 on an expanded scale. Except for the Maxwell Garnett model, the effective permittivities are within the ±0.02 margins (less than ±1 % of the effective values) in the whole composition range. Also the deviations from experimental points are fairly small, as shown in Fig. 3.8. We have calculated the mean square deviations between the model and measured values and listed the results in Fig. 3.8. The least mean deviation occurs for the CPA rule, followed by the Landau-Lifshitz-Looyenga, Bruggeman and Maxwell Garnet

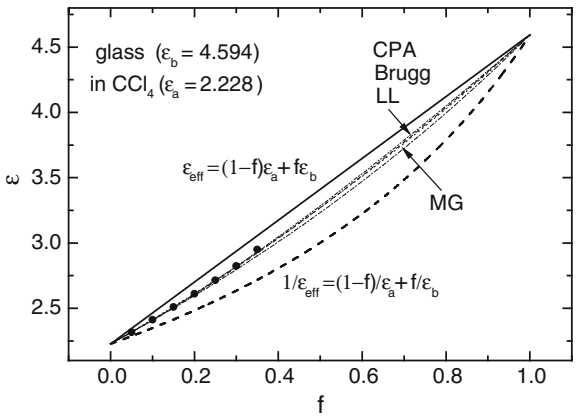

Fig. 3.6 Permittivity of glass spheres dispersed in carbon tetrachloride according to several mixing formulas on the whole range of composition (*lines*); measured data for the volume fraction of glass up to 0.35 (*symbols*)

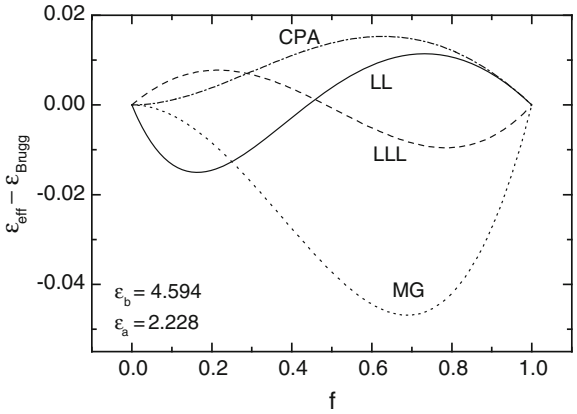

Fig. 3.7 Differences between several mixing formulas for the permittivity of glass spheres dispersed in carbon tetrachloride, data from Fig. 3.6, and the Bruggeman formula

rules. Evidently, the experimental point for the largest value of f might be an outlier; removing it from the data set reduces the mean square deviation of the CPA formula to 0.0015, about a half of the value for the LLL rule.

Another representation of the data is shown in Fig. 3.9. The volume fractions were calculated from the measured value of permittivity and those of the constituents using the same mixing rules as above. Considering the possibility of the data point with the largest value of f being an outlier, the agreement of Bruggeman and CPA with the measured data is excellent. The Maxwell Garnett rule is very good for

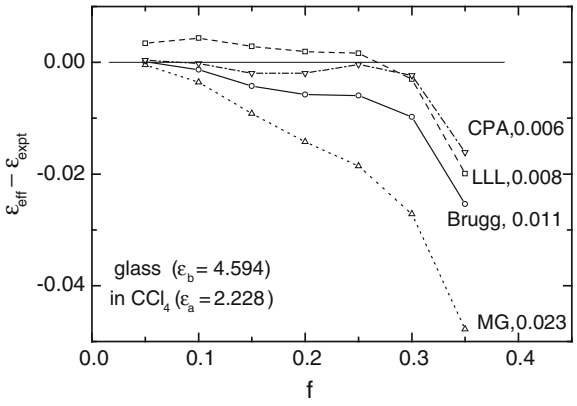

Fig. 3.8 Deviation of the predictions of different mixing formulas from experimental data for glass spheres dispersed in carbon tetrachloride. The mean square deviation for the 7 measured points is given next to the acronym of the mixing formula. The *lines* are guides to the eye

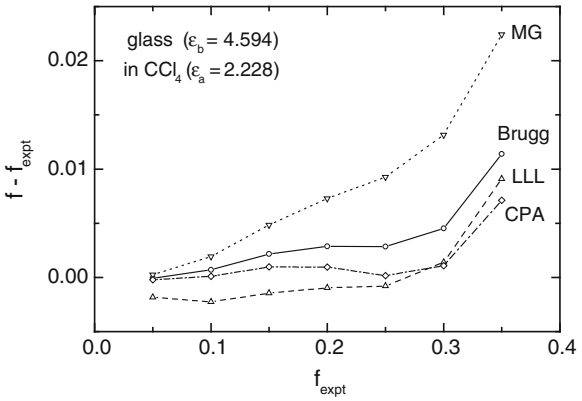

Fig. 3.9 Volume fraction of glass calculated from the measured values of permittivity. The *lines* are guides to the eye

small f, which is expected from the proper account of the screening charges on the glass spheres; however, it overestimates the value of the volume fraction due to the deficiencies of the simplified averaging of Eq. (3.31a,b). The LL rule underestimates the lower values of f; however, it was derived for the condition of small differences of permittivities in the mixture, not satisfied very well in the present case.

The LLL rule of Eq. (3.14) has been derived for a mixture of unspecified geometry, with the only assumption of the isotropy and small variations of the permittivity. The existence of screening charges on inner boundaries is hidden in the manipulation with the divergences of Eqs. (3.8) and (3.9). The corresponding "average screening" lies between the minimum and maximum of the planar interfaces oriented parallel and perpendicular to the electric field, respectively. These two cases would occur for the corresponding orientations of aligned glass platelets dispersed in CCl_4, with the tensor components of the permittivity of Eqs. (3.25) and (3.27). We compare in Fig. 3.10 the compositional dependence resulting from Eq. (3.12), and its approximation of Eq. (3.14), with these two limiting cases. Note that the results of Eqs. (3.12) and (3.14) differ rather markedly; this is obviously due to the large contrast of permittivities of glass and carbon tetrachloride. Further, this way of showing the measured data supports the suspicion of the presence of an outlier (for the largest volume fraction of glass, 0.35).

Another set of experimental data, suitable for testing the EMA mixing rules, has been collected for a dense packing of glass spheres immersed in various liquids [10]. The volume fraction f of soda lime silicate glass (diameter 500 μm) was fixed at the value of 0.605, the pores between the spheres were filled with different liquid immersions. In our notation, the dielectric function of glass inclusions, ε_b, had the value of 7.6. The permittivity of the immersing liquids, ε_a, span the range from 1 (air) to 78.5 (water, at radio frequencies of the order of 1 GHz or smaller used in the measurements). Unfortunately, the uncertainties of the effective permittivity measured using

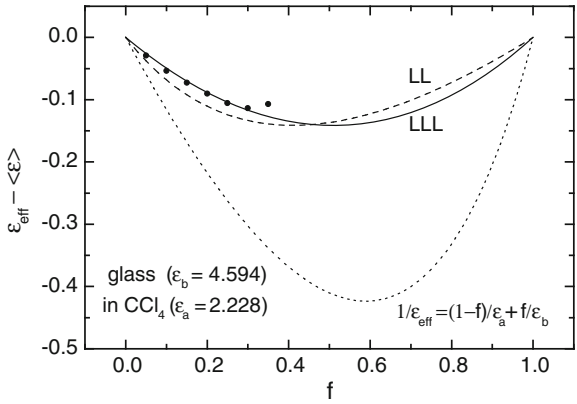

Fig. 3.10 Difference between the effective permittivity of several mixing rules and the volume average of the constituents; LL (*dashed line*) denotes the Landau-Lifshitz formula of Eq. (3.12), LLL (*solid line*) its approximation of Eq. (3.14). Symbols: the difference of measured data from the volume average

the time-domain reflectometry are rather large, the estimate of accuracy quoted in Ref. [10] is ± 0.1. We have digitized the experimental points from Figs. 3.3 and 3.4 of Ref. [10]; they are shown together with the predictions of several mixing rules in Fig. 3.11. Interestingly, the measured points are fairly close to the Maxwell Garnett model for large values of ε_a. A plausible explanation of this fact relies on the averaging procedure of Eq. (3.31), which neglects the fields generated by the surface charges of the spheres. In fact, the large polarizability of the liquids should tend to reduce the contribution of these fields to the average intensity and displacement.

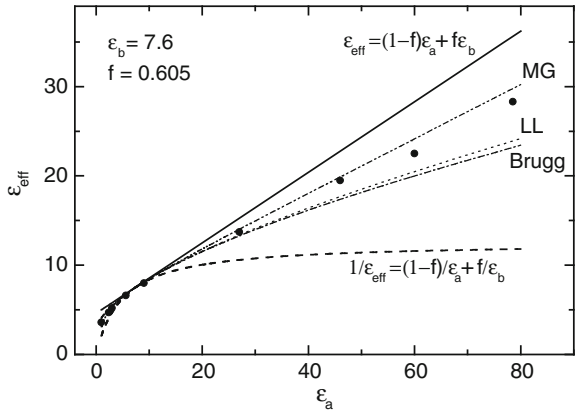

Fig. 3.11 Effective permittivity of glass spheres in different liquids. Experimental data (*symbols*), and several mixing rules (*lines*)

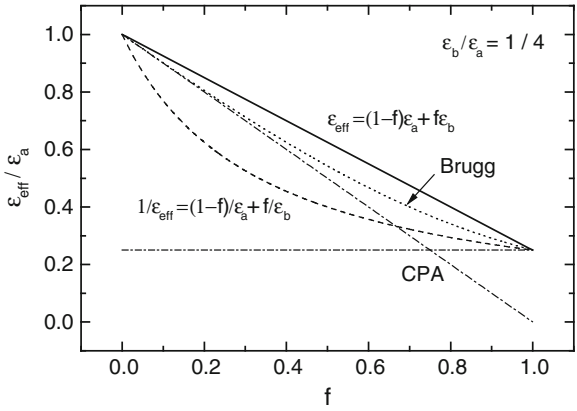

Fig. 3.12 Effective permittivity of several EMA mixing rules for $\varepsilon_b = \varepsilon_a/4$. The *dash-dotted straight lines* are the predictions of the CPA formula of Eq. (3.38)

We have omitted the CPA mixing rule (which provided the best representation of the glass-CCl_4 mixture discussed above) from the comparison of Fig. 3.11. The reason is its failure for large values of the ratio $\varepsilon_a/\varepsilon_b$. An indication of peculiar behavior is linked to the possibility of vanishing denominator in the fraction of Eq. (3.38) for $\varepsilon_b > \varepsilon_a$, or the indefinite expression for the volume fraction f resulting for $\varepsilon_{eff} = \varepsilon_a/4$ (see the last row of the table in paragraph 4). Shown in Fig. 3.12 are the two values of the CPA rule of Eq. (3.38) obtained for $\varepsilon_b = \varepsilon_a/4$. One of the roots of the quadratic Eq. (3.39) is $\varepsilon_{eff} = \varepsilon_a/4$; the remaining one is $\varepsilon_{eff} = \varepsilon_a(1-f)$, coinciding with the linear expansion of Eq. (3.40). Thus, the latter root is usable for small volume fractions f, while it even runs out of the Wiener bounds for larger values of f.

The range of the smaller polarizabilities of the immersion liquids is shown on expanded scales in Fig. 3.13. The CPA, Bruggeman and Landau-Lifshitz predictions are fairly close to one another, while the Maxwell Garnett rule deviates from the three. The measured points lie slightly below the lower Wiener bound for the two largest values of ε_a; the increase with increasing ε_a seems to be closer to that of the CPA, Bruggeman and Landau-Lifshitz models than to the Maxwell Garnett model.

3.6 Testing EMA: Water Solutions of Sucrose

An interesting mixture suitable for the investigation of its optical properties is the water solution of sucrose, as suggested by Feynman in his Lectures [11]. The sucrose molecules, $C_{12}H_{22}O_{11}$, remain stable in aqueous solutions at ordinary temperatures. Further, due to their importance in food industry, the solutions have been measured

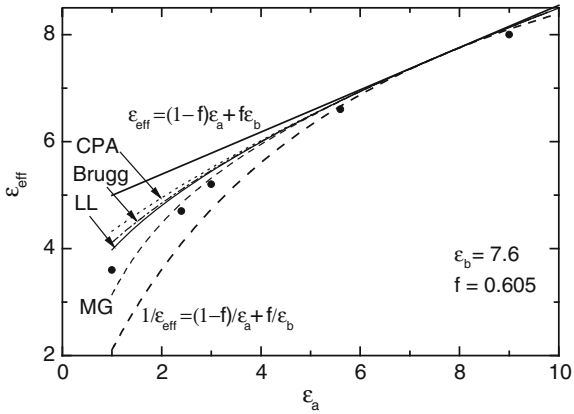

Fig. 3.13 Effective permittivity of glass spheres in different liquids for smaller polarizability of the liquids. Experimental data (*symbols*), and several mixing rules (*lines*)

extensively; reliable, comprehensive datasets in saccharimetry are readily available [12].

Before discussing the optical properties of the solutions, we estimate the volume fractions of their constituents based on the density (mass per unit volume) measurements. The number of molecules in 1 mol of matter is the Avogadro number $N_A = 6.02214 \times 10^{23}$ mol^{-1}. The mass of one solvent (water) molecule and one solute (sucrose) molecule is $m_w = 18.02/N_A$ g and $m_s = 342.3/N_A$ g, respectively. The solution is formed by mixing the masses $M_w = N_w m_w$ and $M_s = N_s m_s$ of the two molecular species, where N_w and N_s are the corresponding numbers of the molecules. The density of the solution is

$$\rho = \frac{N_w m_w + N_s m_s}{V} = c_w m_w + c_s m_s, \tag{3.44}$$

where c_w and c_s are the concentrations of the constituents (i.e., the numbers of molecules per unit volume). Let us assume the total volume V is shared by the corresponding apparent volumes, V_w and V_s, of the constituents, $V = V_w + V_s$. We assume further the apparent volume of the solvent molecule to be that of the pure solvent having the density ρ_w (this assumption is the better the more dilute the solution is). Then, we can rewrite Eq. (3.44) in the following form

$$V_s = \frac{N_w m_w + N_s m_s}{\rho} - \frac{N_w m_w}{\rho_w}. \tag{3.45}$$

Introducing the mass fraction of the solute (a convenient measure of the composition, independent of temperature and pressure),

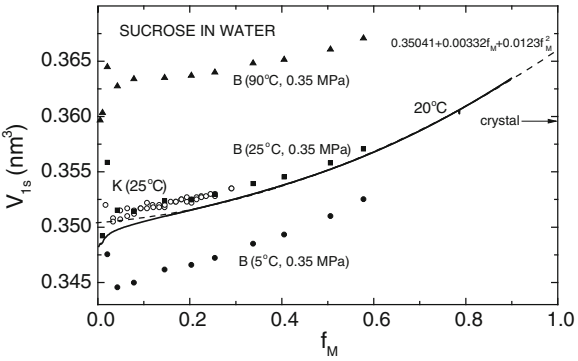

Fig. 3.14 Apparent volume of the sucrose molecule as a function of the mass fraction in water solution, obtained from the density. Tabular data for 20° C of Ref. [12], pp. 343–344 (*thick solid line*); its quadratic approximation (best fit in the range from 0.15 to 0.9, *dashed line*). *Closed symbols* data of Ref. [13] for different temperatures and the pressure of 0.35 MPa. *Open symbols* data of Ref. [14] for 25° C. The *arrow* shows the volume per sucrose molecule in a single crystal at 20° C

$$f_M = \frac{N_s m_s}{N_w m_w + N_s m_s}, \tag{3.46}$$

we use Eq. (3.45) to obtain the apparent volume of one solute molecule:

$$V_{1s} \equiv \frac{V_s}{N_s} = \left(\frac{1}{\rho} - \frac{1 - f_M}{\rho_w}\right) \frac{m_s}{f_M}. \tag{3.47}$$

Shown in Fig. 3.14 is the apparent volume of the sucrose molecule as a function of the mass fraction, obtained from the density data from several sources. We have used the extensive tabulation of Ref. [12] to calculate the dependence shown by the thick solid line in Fig. 3.14. The results are in a fair agreement with the individual data points from two other sources, taking into account the higher temperature of 25° C. As expected, the determination of the apparent volume is rather poor at small mass fractions, when the density of the solution approaches that of the solvent; two close values are subtracted in the parentheses of Eq. (3.45) which magnifies both random and systematic errors.

The increase of the apparent volume with increasing mass fraction indicates the formation of voids adjacent to the sucrose molecules, small enough to prevent filling with water, see the space filling model in Fig. 3.15. The presence of voids should be easily detectable in the optical response of the solutions, provided the dielectric response of water and sucrose molecules was only weakly dependent on the composition of the solution. This assumption has been tested by Feynman [11] using the representation of the water and sucrose molecules by point dipoles, contributing (via their polarizabilities) to the refractive index of the mixture. We will reformulate the problem in terms of the standard EMA picture: the solution is described by the

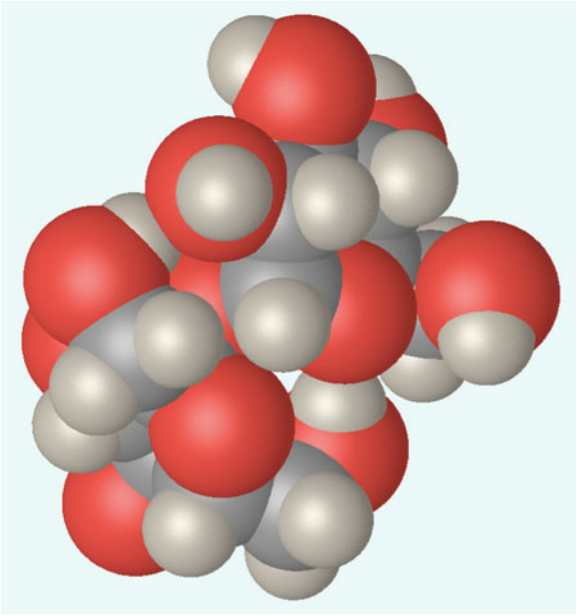

Fig. 3.15 Space filling model of the sucrose $C_{12}H_{22}O_{11}$ molecule, from [15]

three-component mixture with the volume fractions f_w, f_s, and f_v, and permittivities $\varepsilon_w, \varepsilon_s$, and $\varepsilon_v = 1$ of water, sucrose and voids, respectively. We will use the tabulated dependence of the refractive index (i.e., the square root of the permittivity) at the sodium line $\lambda_D = 589.3\,\text{nm}$ at 20 C, covering the compositions from pure water ($f_M = 0$) to $f_M = 0.85$ (85 weight percent of sucrose) [16]. The permittivity of solution increases monotonically from 1.77686 (pure water) to 2.26196 at $f_M = 0.85$, implying the value for the sucrose component in EMA to be below about 2.5; thus, the contrast of the dielectric constants (that of vacuum, water and sucrose) is fairly small, which suggests using the LL or LLL mixing rules of Eqs. (3.12) or (3.14). This choice is further substantiated by the complex geometry of the elongated sucrose molecules and the free volume within their clusters (the averages of the optical fields in the LL approach are independent of the geometry).

Using the LLL mixing formula of Eq. (3.14) for the resulting permittivity ε, we arrive at the following formula for the volume fraction of voids,

$$f_v = \frac{\varepsilon_s^{1/3} - \varepsilon^{1/3}}{\varepsilon_s^{1/3} - 1} - f_w \frac{\varepsilon_s^{1/3} - \varepsilon_w^{1/3}}{\varepsilon_s^{1/3} - 1}. \tag{3.48}$$

The volume fraction of water is provided by the density ρ, using the same reasoning as that in deriving Eq. (3.45):

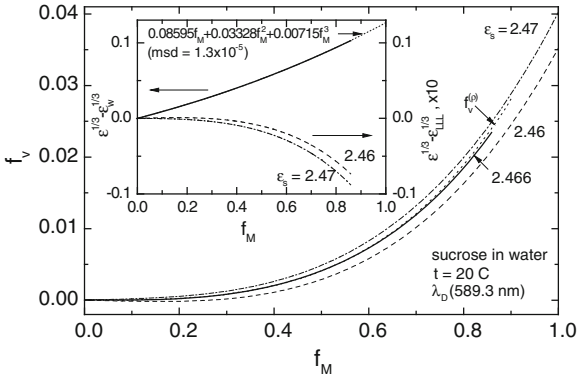

Fig. 3.16 Volume fraction of voids in water solution of sucrose obtained using Eq. (3.48), using ε_s of 2.466 (*solid line*), 2.46 (*dashed line*) and 2.47 (*dash-dotted line*). Dotted line: volume fraction of voids from density, Eq. (3.50). Inset: the difference of the cube root of the dielectric constant from that of pure water (*solid line*), and its polynomial approximant (*dotted line*); magnified (10 times) differences of measured data from the LLL rule for two values of the dielectric constant of sucrose in a two-component mixture (no voids), *dashed* and *dash-dotted lines*

$$f_w = \frac{\rho}{\rho_w}(1 - f_M). \tag{3.49}$$

The only unknown quantity in Eq. (3.48) is the permittivity ε_s, describing the dielectric response of a continuum of sucrose molecules in a hypothetical mixture with no water and no voids. Its value results readily from the plausible requirement of the zero slope of the $f_v(f_M)$ dependence for $f_M \to 0$, which occurs for $\varepsilon_s = 2.466$. This value is larger than the average of the three principal components of the dielectric tensor of the biaxial sucrose crystal (2.427; note that Feynman [11] uses the average of refractive indices to estimate the response of the sucrose component of the solution). Shown in Fig. 3.16 is the volume fraction of voids resulting from Eq. (3.48), using the refractive index (i.e., the square root of the dielectric constant) at 20 C and the wavelength of 589.3 nm given in Ref. [16]. The measured data are represented in the inset of Fig. 3.16 together with its cubic polynomial approximation; the mean square deviation of the two is 1.3×10^{-5} in the whole experimental range of the mass fractions f_M from zero to 0.85. Consequently, we use the polynomial also for the extrapolation of experimental data in order to cover the whole compositional range by the LLL model with ε_s equal to 2.46 (dashed line in Fig. 3.16, negative slope of f_v at $f_M = 0$) and 2.47 (dash-dotted line in Fig. 3.16, positive slope of f_v at $f_M = 0$).

The void fraction can also be estimated from the density ρ of the solution, using the fixed volume of one sucrose molecule from Eq. (3.47) for $f_M \to 0$ throughout the composition range, and attributing the increase of the apparent volume to the presence of the voids. Assuming once more the density of water independent of the composition, we arrive at

$$f_v^{(\rho)} = 1 - \rho \left[\frac{1}{\rho_w} - f_M \left(\frac{1}{\rho_w} - \frac{V_{1s}}{m_s} \right) \right]. \tag{3.50}$$

The resulting void fraction shown in Fig. 3.16 is in a very good agreement with that obtained from the refractive index. Thus, the simple treatment of the packing of the water and sucrose molecules, neglecting the changes of bond lengths and optical polarizabilities with the composition, seems to provide consistent results.

Let us note that the assumption of averaging the microscopic fields of point dipoles using the Clausius-Mossotti relation [11] is very good for dilute solutions. In fact, the conceptually similar treatment of EMA described above results in the volume fraction of voids smaller than 0.001 for the mass fraction of sucrose less than 0.32. On the other hand, the presence of voids is clearly indicated in denser solutions, and discrepancies of a few percent are observed in the EMA description of the dielectric function when using the simplest two-component picture.

The concentrated sucrose solutions were studied by molecular dynamics simulations in [17]. These calculations suggested a non-monotonic dependence of the free volume fraction on the compositions, which is absent in the data of Fig. 3.16 resulting from both density and refractive index. A further notice concerns the temperature dependence of Fig. 3.14: the increase of the free volume with increasing sucrose fraction is steeper at higher temperatures. This indicates the role of dynamical effects in filling the voids between clustered sucrose molecules with water.

Of course, EMA has to be used with caution. Substantial deviations from the simple mixing are expected in the spectral range of strong absorption (of both sucrose and water); the spectral shifts of molecular absorption bands due to the changes of environment of each molecule when changing concentration would be absent in the model spectra. The simplest EMA approach would also fail if it was used in treating the light scattering by the solutions [18]. However, the predictions of EMA described above are very good in predicting the refractive index in the transparent range, in spite of the very small size of the sucrose molecule ($V_{1s} \sim 0.35\,\mathrm{nm}^3$ at room temperature).

3.7 Differences Between Mixing Rules for Binary Dielectric Mixtures

The choice of a mixing rule in a particular situation need not be obvious. It is therefore desirable to estimate the differences between various plausible possibilities. This is easily accomplished in the simplest case of binary mixtures possessing real components of permittivity. Different rules provide differing compositional dependences of the effective permittivity, interpolating between the two constituents. The simplest linear interpolation is exact (in the long-wavelength limit) for layers parallel to the electric intensity, the perpendicular orientation is properly described by addi-

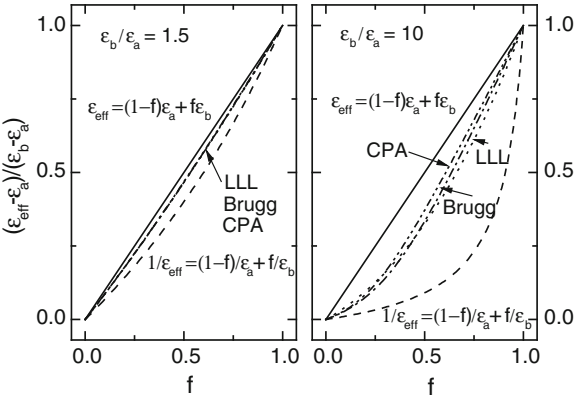

Fig. 3.17 Normalized difference of the effective permittivity of binary mixtures from that of one of the components, ε_a, for $\varepsilon_b = 1.5\,\varepsilon_a$ (*left panel*) and $\varepsilon_b = 10\,\varepsilon_a$ (*right panel*). The mixing rules: Eq. (3.25), *solid line*; Eq. (3.27), *dashed line*; Eq. (3.14), *dotted line*; Eq. (3.36), *dash-dotted line*; Eq. (3.38), *dash-dot-dotted line*

tive inverse permittivities of Eq. (3.27). These two limiting cases are usually called *Wiener bounds* for two-phase mixtures of any microstructure.

The Wiener bounds and the effective permittivities of three selected mixing rules are shown in Fig. 3.17 for two values of $\varepsilon_b/\varepsilon_a$. We have chosen the CPA and Bruggeman rules for spherical inclusions, and the LLL formula for a small difference of the permittivities. For the smaller contrast, the bounds are fairly close and the three rules are indistinguishable on the scale of the figure. However, the large relative value of ε_b in the right panel of Fig. 3.17 shifts the lower bound rather significantly, since the smaller value ε_a becomes more important. In addition, the remaining mixing rules deviate markedly from each other. It should be reemphasized that the LLL rule has been derived for small values of $\varepsilon_b/\varepsilon_a$; we have included it here in order to draw the attention to a possible "accidental" success of any mixing rule. For example, the predictions of CPA and LLL rules coincide for $f \approx 0.29$ for the ratio of permittivities as high as 10.

The differences between the selected mixing rules are better seen on expanded (logarithmic) scales of Fig. 3.18. The difference between the LLL and CPA rule (left panel of Fig. 3.18) crosses zero at $f \approx 0.29$ in a broad range of the dielectric contrasts. At the same time, the CPA and Bruggeman rules agree within less than one percent of the difference between the constituents.

All of the tested rules agree within a few percent of the difference between the permittivities of the components when the latter does not exceed 10. Moreover, the mutual agreement is much better for dilute mixtures (small values of f); this is expected since the averaged fields become less sensitive to the properties of inclusions and their interactions.

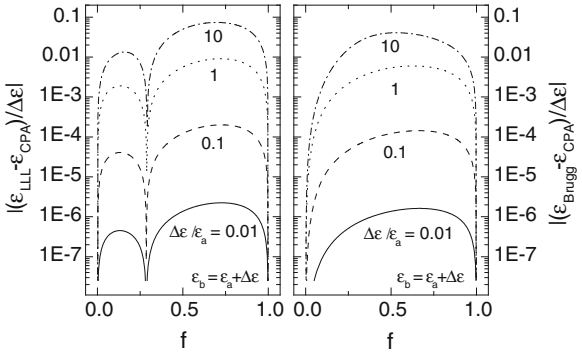

Fig. 3.18 Normalized difference of the effective permittivities of binary mixtures calculated from the rules used in Fig. 3.17: LLL and CPA (*left panel*), Bruggeman and CPA (*right panel*)

3.8 Exact Solutions and EMA for Layered Structures

Layered structures of the type shown in Fig. 3.2 represent a convenient system for evaluating quantitatively the approach of effective medium. Namely, the optical fields can be computed exactly for incident plane waves using the scheme of transfer matrices [19]; moreover, analytical results are available for derivatives of the field amplitudes and ellipsometric quantities, enabling a very efficient fitting of measured data [20]. We show here examples of exact results and their approximation using effective medium approach. Let us start with the positional dependence of the field intensity

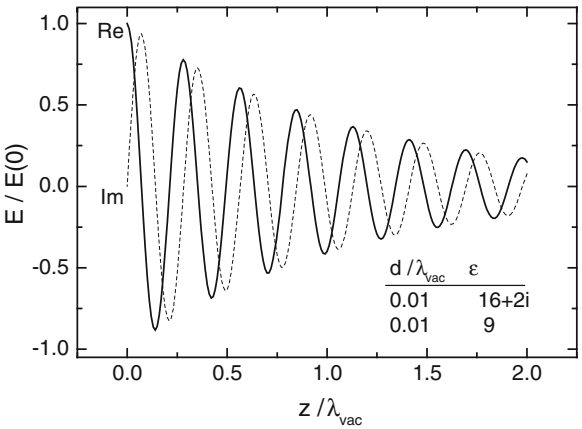

Fig. 3.19 Complex amplitude of the electric intensity of a plane wave propagating along the z axis in the layered system consisting of repeated pairs of films specified by the thickness d and the dielectric function ε

shown in Fig. 3.19. The wave, travelling in the z direction, is damped due to the absorption in one of the layers in the repeated pairs. The electric intensity is parallel to the interfaces, i.e., the angle of incidence in Fig. 3.2 is zero. The exact solution is composed from linear combinations of plane waves in each of the layers, with the electric intensity continuous across the interfaces and the electric displacement undergoing step-like changes. The appropriate effective permittivity is the simple volume average with no screening, Eq. (3.25). The damped plane wave solving the propagation in the effective medium is indiscernible from the exact solution at the scale of Fig. 3.19. The reason is the smallness of the thickness of individual layers with respect to the wavelength of the optical field. The latter is about λ_{vac}/n_{eff}, with the effective refractive index of $\sim$3.54 resulting from the volume average of the two permittivities of the mixture. The detailed comparison of the exact and approximate fields shown in Fig. 3.20 reveals a subtle relative difference of the order of 10^{-3}. Even this small difference could be observed via differences in interference patters observed in light reflected from or transmitted by a film of suitable thickness made from this model metamaterial. On the other hand, the differences diminish with decreasing d/λ ratio.

This kind of differences of the inner fields in the metamaterial becomes fairly easily observable in ellipsometric measurements. We show in Fig. 3.21 the spectra of the standard ellipsometric angles computed for different values of d/λ_{vac}, where d is the total thickness of the layered metamaterial of Fig. 3.19. We have used the repeated pairs of the $\lambda_{vac}/1000$ films of the two different dielectric functions, kept constant throughout the calculation of the spectra, calling the metamaterial a "superlattice" (SL). The substrate has been chosen to be the material with the complex permittivity $16 + 2i$, the more polarizable component of the mixture. Because of the large

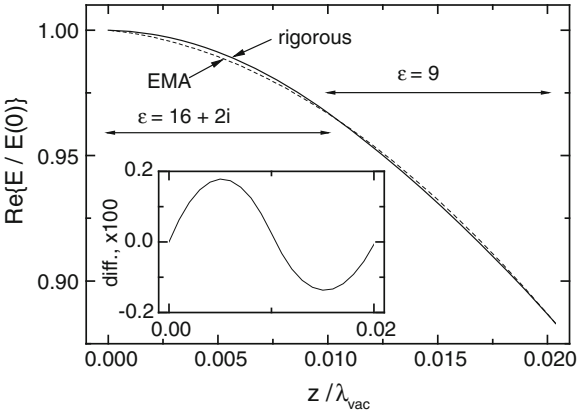

Fig. 3.20 A detail of the electric intensity of Fig. 3.19 obtained by solving rigorously the wave equation in the film stack (*solid line*) and in the appropriate effective medium (*dashed line*). The extent of neighboring individual layers is indicated by the *horizontal arrows*. The *inset* shows the difference between the two intensities on an expanded vertical scale

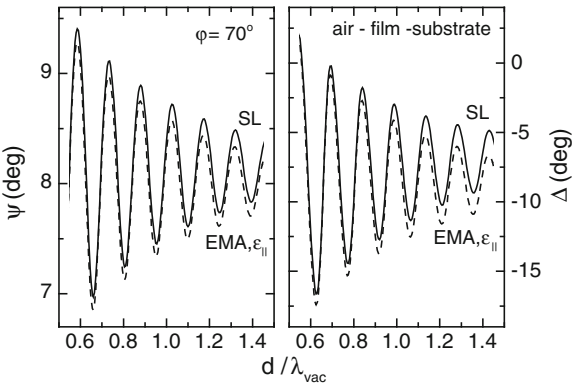

Fig. 3.21 Ellipsometric angles, (ψ, *left panel*) and (Δ, *right panel*), computed for a layer of thickness d, made of the metamaterial of Fig. 3.19 with $d_1 = d_2 = \lambda_{vac}/1000$, at the angle of incidence of 70°. *Solid line* exact solution; *dashed line* effective medium approximation, using the isotropic dielectric function along the interfaces

refractive index of the metamaterial, the optical wave is refracted very close to the z direction, and the usual approach is to neglect the anisotropy and use the parallel component of the dielectric function for the appropriate effective medium. The exact and EMA calculations produce similar interference patterns, displaying a pronounced decrease of the amplitude with increasing ratio d/λ_{vac}, due to the absorption in the metamaterial. The EMA calculation deviates from the exact result for the following two reasons: the neglected anisotropy, and the finite values of d_1 and d_2. A closer look at the increase of the differences for decreasing wavelength identifies the second reason as the decisive one.

In order to identify potential problems caused by a too coarse structure of the mixture compared to the wavelength, we have performed the exact calculations of the ellipsometric spectra for different thicknesses of the constituent bilayers, keeping the total thickness d of the metamaterial fixed. In other words, we have used the appropriate number of repetitions of the basic bilayer motif, $d/(d_1 + d_2)$.The results shown in Fig. 3.22 demonstrate a fairly high sensitivity of ellipsometry to the fineness of the mixture; as usual, the phase shift Δ is more sensitive. Note that considerable changes from the behavior of a "true mixture" occur for the individual layer thicknesses well below one percent of the wavelength in the effective medium.

The dramatic changes seen for thicker constituent layers are due to the interferences in the stack of layers with the high and low index of refraction. In fact, the thickness of individual layers close to $\lambda/4$ leads to the appearance of Bragg-like bands of increased reflectivities and corresponding changes in the relative phase shifts.

We can readily transform these model calculations into practical guidelines for the applicability of the effective medium (i.e., continuum) approximation of the layered metamaterial. Namely, at the representative vacuum wavelength of the visible range,

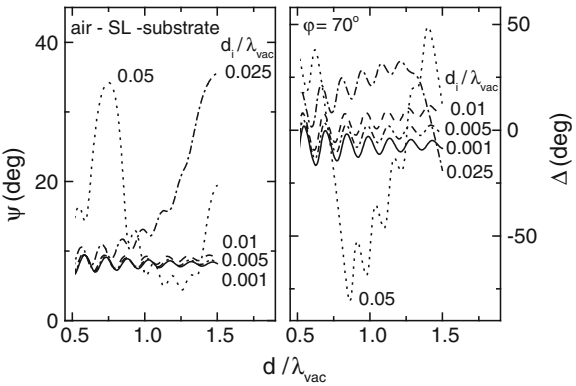

Fig. 3.22 Ellipsometric angles, (ψ, *left panel*) and (Δ, *right panel*), computed for a layer of fixed thickness d, made of the metamaterial of Fig. 3.19 with different values of $d_1 = d_2$, at the angle of incidence of 70°

500 nm, we observe easily detectable (at least one tenths of a degree in ψ, and one degree in Δ) changes for the individual layer thicknesses as low as 2 nm in this particular metamaterial. Of course, this value scales with the wavelength in the mixture.

This level of sensitivity is related to a possible detection of surface or interface roughness in ellipsometric measurements. In fact, the representation of the surface roughness as the presence of an overlayer composed of the topmost material and voids is usually a plausible approximation explaining the measured data. Similarly, the interface roughness can be modeled by inserting a thin layer of mixed composition. These transition layers are graded; due to the usually small extent of the grading, the approximation by a single homogeneous layer of intermediate composition is suitable. However, without independent information concerning the geometry of these mixtures, values of film thicknesses and compositions derived from measured data should be used with care.

3.9 Resonant Behavior of EMA Mixtures

When selecting properly the individual contributions of the constituents of an EMA mixture, we can arrive at a spectacular behavior of the effective optical response; the latter can be traced down to the spectacular behavior of local fields. We outline here the simple cases having analytical solutions, based on the constant field inside an isolated ellipsoid in an infinite host medium as described by Eq. (3.29). Namely, the field intensity inside the ellipsoid becomes infinite whenever

$$\frac{\varepsilon_b}{\varepsilon_a} = 1 - \frac{1}{L_u} \in (-\infty, 0\rangle. \tag{3.51}$$

According to the value of the depolarization factor L_u of Eq. (3.30), this divergence occurs in particular in a

- sphere: $u = v = w$, $L_u = 1/3$, for $\varepsilon_b = -2\varepsilon_a$;
- cylinder, field perpendicular to its axis: $u = v$, $w \to \infty$, L_u =1/2, for $\varepsilon_b = -\varepsilon_a$;
- slab, field perpendicular to the interface: $v = w \to \infty$, $L_u = 1$, for $\varepsilon_b = 0$.

To fulfill this condition, the permittivity of the inclusion has either to vanish or to be of the opposite sign as that of the host. Since the response functions are frequency dependent, the diverging (in practice, very large) field intensities can only occur in narrow spectral ranges, i.e., they exhibit resonant behavior. Let us note that the above condition for the slab is related to the occurrence of the surface plasmon resonance, achieved by using a thin metallic film and the obliquely incident, p-polarized wave; the enhanced fields occur for $\varepsilon_b \approx 0$ in the metal.

Assuming a dilute mixture (the volume fraction $f \ll 1$) of aligned ellipsoids, the Maxwell Garnett formula of Eq. (3.32a) leads to a diverging dielectric function for

$$\frac{\varepsilon_b}{\varepsilon_a} = 1 - \frac{1}{L_u(1-f)}, \tag{3.52}$$

which is close to the condition of diverging field of Eq. (3.51). In the case of flat interfaces perpendicular to the field, the effective dielectric function can be expanded in the form

$$\varepsilon_{eff} \approx \varepsilon_a(1+f) - \frac{\varepsilon_a^2}{\varepsilon_b} f, \tag{3.53}$$

leading to a divergence whenever ε_b crosses zero (in practice, its imaginary part being small and the real part crossing zero). The spectral lineshape of the resonance, proportional to negative inverse of ε_b, is almost independent of f; it is multiplied by the squared permittivity of the host material, which is large for highly polarizable materials.

The resonance condition of Eq. (3.52) is actually exact for the field perpendicular to flat interfaces (i.e., $L_u = 1$). In fact, the effective dielectric function of Eq. (3.27) diverges for

$$\frac{\varepsilon_b}{\varepsilon_a} = -\frac{f}{1-f} \tag{3.54}$$

at any volume fraction f. With equal volume fractions of one half (i.e., equal film thicknesses), the resonance occurs for $\varepsilon_b = -\varepsilon_a$. The opposite signs of the permittivitites have been achieved by a proper doping of one of the components of a semiconductor superlattice [21], as shown in Fig. 3.23. The undoped AlInAs alloy possesses an (almost constant) positive permittivity ε_a throughout the mid-infrared

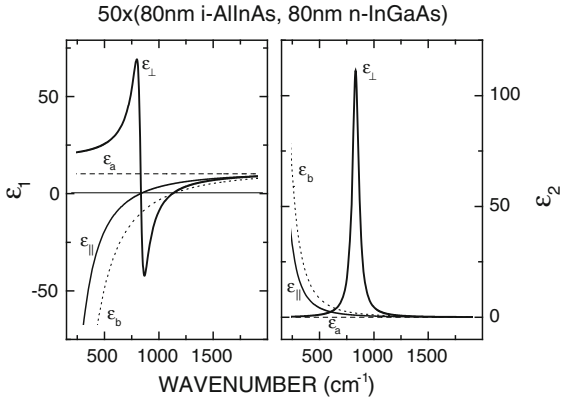

Fig. 3.23 Real (*left panel*) and imaginary (*right panel*) parts of the model dielectric functions of the layered heterostructure formed by alternating components (insulating, ε_a) and (a single Drude term on a constant real background, ε_b) of equal thicknesses. The effective dielectric functions for the electric field parallel and perpendicular (*solid lines*) to the film interfaces

(MIR) range, while the n-type InGaAs alloy has the negative-valued real part of its permittivity, ε_b, up to the wavenumber of about 1130 cm^{-1}, due to the Drude-like contribution of free electrons. The model lineshapes of Fig. 3.23 are based on ellipsometric measurements [22] performed on a superlattice layer (lattice-matched to its InP substrate), exhibiting negative refraction in MIR [21]. With equal film thicknesses, the effective medium response for the field perpendicular to the interfaces displays a strong resonance at 832 cm^{-1}, and a band of negative real part of permittivity from 836 to 1125 cm^{-1}.

Another example of the resonance governed by Eq. (3.54) is the "transverse plasmon" in the c-axis response of superconducting cuprates [23]. In this case, the resonant behavior observed in the far-infrared range is more damped due to the energy losses of normal-state carriers.

The averaging procedure pertinent to the EMA treatment of finely structured metamaterial is instructive also for the strongly anisotropic layer stack of Fig. 3.23. In fact, it explains in simple terms the effect of negative refraction occurring in a fairly broad range of wavenumbers [22]. The averaging procedure is shown in detail for a selected pair of undoped (positive permittivity) and doped (negative permittivity) layers. With an arbitrary selection of the electric field intensity in the former layer, we find all of the intensities and displacements as follows:

$$\begin{aligned} D_{ax} &= \varepsilon_a E_{ax}, \quad D_{az} = \varepsilon_a E_{az} && \text{(isotropic material a)},\\ E_{ax} &= E_{bx}, \quad\ D_{az} = D_{bz} && \text{(crossing the interface)},\\ D_{bx} &= \varepsilon_b E_{bx}, \quad E_{bz} = D_{bz}/\varepsilon_b && \text{(isotropic material b)}. \end{aligned}$$

Further, the averaging assuming the thicknesses d_a, d_b, $d = d_a + d_b$, and the volume fractions $f_a = d_a/d, f_b = d_b/d = 1 - f_a$, leads to

$$\begin{aligned}
\langle E_x \rangle &= f_a E_{ax} + f_b E_{bx} = E_{ax}, \\
\langle E_z \rangle &= f_a E_{az} + f_b E_{bz} = (f_a + f_b \varepsilon_a/\varepsilon_b) E_{az}, \\
\langle D_x \rangle &= f_a D_{ax} + f_b D_{bx} = (f_a \varepsilon_a + f_b \varepsilon_b) E_{ax}, \\
\langle D_z \rangle &= f_a D_{az} + f_b D_{bz} = D_{az} = \varepsilon_a E_{az},
\end{aligned}$$

i.e., to the components of the dielectric tensor of the resulting effective medium:

$$\begin{aligned}
\langle D_x \rangle &= \varepsilon_{||} \langle E_x \rangle = (f_a \varepsilon_a + f_b \varepsilon_b) \langle E_x \rangle, \\
\langle D_z \rangle &= \varepsilon_{\perp} \langle E_z \rangle = \frac{1}{f_a/\varepsilon_a + f_b/\varepsilon_b} \langle E_z \rangle.
\end{aligned}$$

This averaging procedure assumes constant fields within each layer, in other words, film thicknesses negligible compared with the wavelength. The average flow of energy, shown also in Fig. 3.24, occurs in the "negative" direction.

The description of the doped multilayer within the EMA framework has been tested by performing MIR ellipsometric measurements [22]. The good agreement of the measured and model spectra (no fitting, the nominal layer thicknesses and a guess of

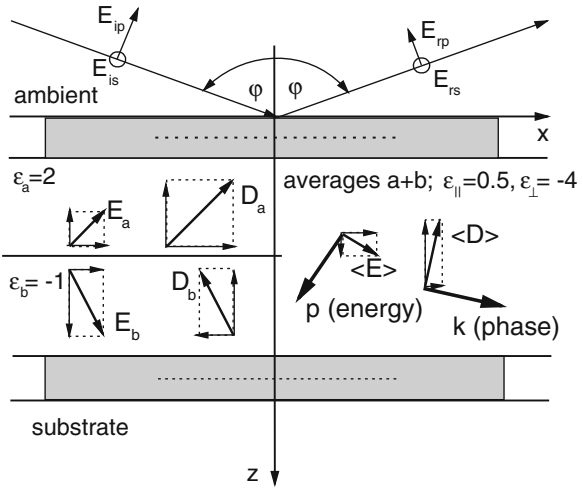

Fig. 3.24 Electric field (E) and displacement (D) amplitudes of a plane wave inside a pair of selected neighboring layers (of equal thicknesses) of the anisotropic layered material, differing by the sign of their real permittivities (*left part*). The *right part* volume averages of the fields, the directions of the propagation of the constant-phase planes (k) and the flow of energy (Poynting vector, p), perpendicular to $\langle D \rangle$ and $\langle E \rangle$, respectively, are shown by the *thick arrows*

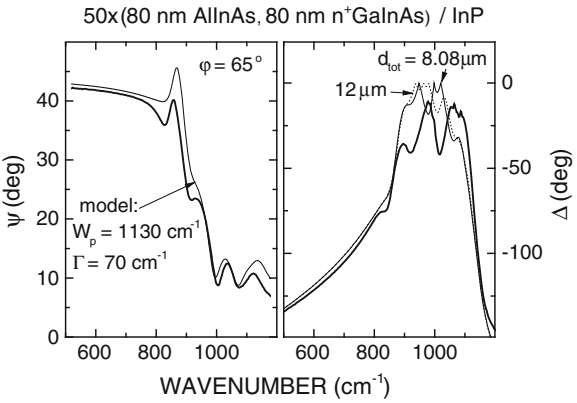

Fig. 3.25 Measured (*thick solid lines*) and model (*thin solid lines*) spectra of the ellipsometric angle ψ (*left panel*) and Δ (*right panel*) at the angle of incidence of 65°. The model calculation used a single Drude term with the indicated parameters. An additional model spectrum of Δ was calculated for the total thickness of the metamaterial layer of 12 μm (*dotted line*)

the Drude parameters of the doped material have been used in the model) confirms the usefulness of the EMA picture.

The individual layer thicknesses of 80 nm are small compared with the wavelength if MIR light in the metamaterial. On the other hand, the interference pattern with the period of about 100 cm^{-1} results from the coherent reflections within the total thickness of 8080 nm of the superlattice. We have tested this interpretation by calculating the model spectra of Δ for two values of the total thickness of the metamaterial layer. Note that the spectra of Δ are folded to the range from -180 to 0° (due to the rotating-analyzer measurement setup, which is unable to determine the sign of Δ). The denser interference pattern obtained for the larger total thickness confirms our assumption (Fig. 3.25).

3.10 Conclusions

The approximate treatment of mixtures using effective medium approach is simple and attractive, as it can capture important properties of nanostructured materials. We would encourage using it, whenever the underlying assumptions are fulfilled. The applicability of any specific EMA formula should be assessed carefully, and the level of uncertainties estimated.

It might be surprising to find a consistent EMA picture of the water solutions of sucrose in the visible spectral range, remembering the apparent volume of one sucrose molecule of about 0.35 nm^3. Further, the individual layers in a semiconductor superlattice might be as thick as ∼0.1 μm and still form a proper component in the EMA

continuum in the mid-infrared range, and even provide a plausible explanation of the negative refraction. We could easily find a failure of the EMA models for these systems in other circumstances; however, this would not be a defect of the approach, but that of its improper use.

References

1. J.C. Maxwell, *A Treatise on Electricity and Magnetism*, vol. I, 3rd edn. (Clarendon Press, Oxford, 1904), Sect. 314
2. L.D. Landau, E.M. Lifshitz, *Electrodynamics of Continuous Media*, 2nd edn. (Pergamon Press, Oxford, 1984), Sect. 9
3. H. Looyenga, Physica **31**, 401 (1965)
4. J.D. Jackson, *Classical Electrodynamics* (Wiley, New York, 1962)
5. J.A. Stratton, *Electromagnetic Theory* (McGraw-Hill, New York, 1941)
6. J.C.M. Garnett, Philos. Trans. R. Soc. Lond. **203**, 385 (1904)
7. D.E. Aspnes, Am. J. Phys. **50**, 704 (1982)
8. D.A.G. Bruggeman, Ann. Phys. (Leipzig) **24**, 636 (1935)
9. A. Sihvola, *Electromagnetic Mixing Formulas and Applications* (IEE, Stevenage, 1999)
10. D.A. Robinson, S.P. Friedman, J. Non-Cryst. Solid **305**, 261 (2002)
11. R.P. Feynman, R.B. Leighton, M. Sands, *The Feynman Lectures on Physics*, vol. II (Addison-Wesley, Boston, 1964), Sect. 32–5
12. *International Critical Tables of Numerical Data, Physics, Chemistry and Technology*, vol. 2, First Electronic Edition (Knovel, Norwich, New York, 2003), pp. 334–355
13. B.R. Brown et al., J. Chem. Thermodyn. **37**, 843 (2005)
14. K. Kiyosawa, Bull. Chem. Soc. Jpn. **61**, 633 (1988)
15. http://www.crystmol.com/structures/Sucrose_SpaceFilling.jpg
16. www.icumsa.org, ICUMSA Method SPS-3 (2000)
17. V. Molinero et al., Chem. Phys. Lett. **377**, 469 (2003)
18. M. Kazsuba et al., J. Nanopart. Res. **10**, 823 (2008)
19. F. Abeles, Annls Phys. **5**, 596 (1950)
20. J. Humlíček, Optica Acta **30**, 97 (1983)
21. A.J. Hoffman et al., Nat. Mater. **6**, 946 (2007)
22. J. Humlíček, Thin Solid Films **519**, 2655 (2011)
23. J. Chaloupka, D. Munzar, J. Humlíček, *Advanced mueller ellipsometry instrumentation and data analysis*, ed. by M. Losurdo, K. Hingerl, Ellipsometry at the nanoscale